ACS APPLIED MATERIALS & INTERFACES

www.acsami.org

Research Article

# Modulation of Charge Transport at Grain Boundaries in $SrTiO_3$: Toward a High Thermoelectric Power Factor at Room Temperature

Jianyun Cao, Dursun Ekren, Yudong Peng, Feridoon Azough, Ian A. Kinloch,* and Robert Freer*

Cite This: *ACS Appl. Mater. Interfaces* 2021, 13, 11879–11890

Read Online

ACCESS | Metrics & More | Article Recommendations | Supporting Information

**ABSTRACT:** Modulation of the grain boundary properties in thermoelectric materials that have thermally activated electrical conductivity is crucial in order to achieve high performance at low temperatures. In this work, we show directly that the modulation of the potential barrier at the grain boundaries in perovskite $SrTiO_3$ changes the low-temperature dependency of the bulk material's electrical conductivity. By sintering samples in a reducing environment of increasing strength, we produced $La_{0.08}Sr_{0.9}TiO_3$ (LSTO) ceramics that gradually change their electrical conductivity behavior from thermally activated to single-crystal-like, with only minor variations in the Seebeck coefficient. Imaging of the surface potential by Kelvin probe force microscopy found lower potential barriers at the grain boundaries in the LSTO samples that had been processed in the more reducing environments. A theoretical model using the band offset at the grain boundary to represent the potential barrier agreed well with the measured grain boundary potential dependency of conductivity. The present work showed an order of magnitude enhancement in electrical conductivity (from 85 to 1287 S $cm^{-1}$) and power factor (from 143 to 1745 $\mu W$ $m^{-1}$ $K^{-2}$) at 330 K by this modulation of charge transport at grain boundaries. This significant reduction in the impact of grain boundaries on charge transport in $SrTiO_3$ provides an opportunity to achieve the ultimate "phonon glass electron crystal" by appropriate experimental design and processing.

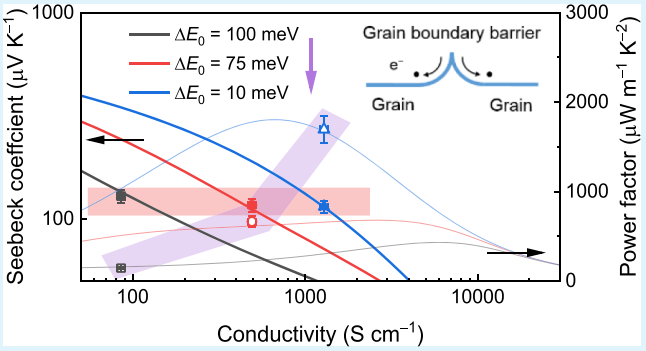


**KEYWORDS:** *$SrTiO_3$, thermoelectric, grain boundary, modulation, charge transport*

## INTRODUCTION

Grain boundaries exist in all polycrystalline materials and have significant impact on, and may dominate, the overall structural and functional properties of the material.[1−4] The modulation of grain boundaries' characteristics (e.g., grain size, local elementary composition, chemical state, etc.) provides an opportunity to tune bulk properties including mechanical strength,[5] electronic and ionic conductivity,[3,6−8] photovoltaic efficiency,[4] and thermal conductivity.[9] Recently, interest has grown in the optimization and enhancement of thermoelectric properties of inorganic compounds via grain boundary (GB) engineering.[1,3,6,7]

Thermoelectric materials that can generate electricity efficiently from waste heat are of considerable interest in the development of future sustainable society.[10−13] Particularly, in the forthcoming age of internet of things enabled by the 5G network, the thermoelectric generator that operates at room or near room temperatures can (i) convert the low-grade waste heat (30−250 °C) generated by electronic devices to electricity and (ii) power up wearable and mobile sensors using human body heat.[14−16] For thermoelectric materials, the energy conversion efficiency is evaluated by the dimensionless figure of merit ($ZT$), which is determined by the equation $ZT = (S^2\sigma/\kappa)T$, where $S$, $\sigma$, $\kappa$, and $T$ are the Seebeck coefficient, electrical conductivity, thermal conductivity, and absolute temperature, respectively; thus, we need to maximize charge transport and minimize thermal transport.[11] The presence of grain boundaries affects both the power factor ($S^2\sigma$) and the thermal conductivity of bulk materials.[1,9,17] For some materials, such as $SrTiO_3$ and $Mg_3Sb_2$, the buildup of electrostatic potential at the GB acts as a barrier for charge carrier transport, limiting the overall carrier mobility, particularly at and near room temperature.[18−21] Meanwhile, the GB interface is itself a type of lattice defect assemblage that assists in the reduction of thermal conductivity.[9,22] These conflicting effects of grain boundaries on electrical and thermal transport present major challenges in the development of high-performance nanocrystalline thermoelectric materials operating over a range of temperatures. Therefore, modulation of grain

Received: December 7, 2020
Accepted: January 28, 2021
Published: March 4, 2021





https://dx.doi.org/10.1021/acsami.0c21699
*ACS Appl. Mater. Interfaces* 2021, 13, 11879−11890

boundaries, which can reduce their impact on charge carrier transport while retaining their ability to suppress lattice thermal conductivity, is in demand.

Recent work on n-type $SrTiO_3$-based thermoelectric ceramics showed that the thermally activated behavior of low-temperature electrical conductivity disappeared with the use of certain processing conditions (temperature, oxygen partial pressure, etc.) and/or after incorporation of additives (e.g., graphene).[3,18,22,23] The analysis of energy- and carrier concentration-independent weighted mobility showed that charge transport in polycrystalline $SrTiO_3$ can approach that of a single crystal.[7] Generally, this single-crystal-like electrical conductivity at low temperature is attributed to the decrease in GB resistance with the reduction of the built-in potential barrier at the grain boundaries.[3,6,7,18] Localized changes in GB chemistry and structure (elementary composition, chemical state, etc.) are thought to be the primary reasons for the reduction of the potential barrier at the grain boundaries.[3] However, to date, there has been no direct evidence, either experimental or theoretical, that links the GB potential with the change in temperature dependency of conductivity in thermoelectric materials.

A recently developed two-phase model,[1] which treated the GB as a separate phase with a band offset from the neutral grain phase, was able to capture the measured temperature-dependent electrical conductivity in $Mg_3Sb_2$-based compounds. The band offset of the GB phase acted as a potential barrier for carrier transport. This two-phase model showed good agreement with the grain size-dependent conductivity in $Mg_3Sb_2$-based compounds,[1] as the contribution of GB resistance becomes much less dominant at larger grain sizes. However, perovskite $SrTiO_3$-based ceramics, with comparably small grain sizes (0.5−5 $\mu$m) exhibited distinctly different temperature dependencies of conductivity, showing either thermally activated or single-crystal-like behavior.[22,24] This inconsistency in charge transport in $SrTiO_3$-based ceramic with similar grain sizes strongly indicates that the intrinsic GB properties (e.g., built-in potential) vary from sample to sample, even for samples with a similar stoichiometry.

In this work, by combining experimental results with theoretical modeling, we directly show that the modulation of the potential barrier at grain boundaries effectively switches the low-temperature conductivity of La-doped $SrTiO_3$ from thermally activated to single-crystal-like behavior. We begin with the prediction of temperature-dependent electrical conductivity using the recently developed two-phase model; by lowering the magnitude of the band offset at the GB (i.e., height of the potential barrier), the low-temperature electrical conductivity changes from thermally activated to single-crystal-like behavior. We experimentally modulated the GB properties of $La_{0.08}Sr_{0.9}TiO_3$ (LSTO) ceramic by control of processing conditions. The as-prepared LSTO ceramic samples showed a gradual change in low-temperature electrical conductivity from the thermally activated to single-crystal type, with an order of magnitude increase in electrical conductivity and power factor at 330 K. The experimental results fit well with the two-phase model, showing good agreement for the dependency of electrical conductivity on GB potential. Moreover, the reduction in GB potential was confirmed by imaging the surface and analysis of local potential by Kelvin probe force microscopy (KPFM).

## EXPERIMENTAL SECTION

**Materials.** The starting powders of $TiO_2$ (>99.9%) and $SrCO_3$ (>99.9%) were obtained from Sigma-Aldrich (Gillingham, Dorset, UK). $La_2O_3$ powder (>99.99%) was obtained from PI-KEM (Magnus, Tamworth, UK). Isopropanol was supplied by Sigma-Aldrich (Gillingham, Dorset, UK), and the graphene nanoplatelets (GNPs), grade M25, were obtained from XG science (Lansing, USA).

**Preparation of $La_{0.08}Sr_{0.9}TiO_3$ (LSTO) Powder.** The A-site deficient $La_{0.08}Sr_{0.9}TiO_3$ ceramic powder was prepared by a solid-state reaction approach. The starting powders of $TiO_2$, $SrCO_3$, and $La_2O_3$ were weighed according to the stoichiometry before mixing. The $La_2O_3$ powder was calcined in air at 1173 K for 6 h to remove moisture before weighing. After wet milling in isopropanol for 24 h using zirconia ball milling media, the well-mixed powders were dried at 90 °C for 24 h. The solid-state reaction to form LSTO was conducted in an alumina crucible at 1473 K in air for 8 h. The as-prepared LSTO powder was subjected to planetary milling (Retsch planetary ball mill PM 100) at 350 rpm for 4 h to reduce the average particle size to ∼590 nm.

**Sintering of LSTO Ceramics.** The bulk LSTO ceramics were prepared by conventional pressureless sintering. A uniaxial press was used to compact the LSTO powders into green body pellets 15 or 20 mm in diameter and 5 mm in height. The as-formed pellets were densified at 1700 K under three types of conditions with an increasingly strong reducing environment, namely, (1) Ar-$H_2$-5%, (2) Ar-$H_2$-5% and sacrificial carbon powder but not in direct contact with the LSTO green body, and (3) Ar-$H_2$-5% and sacrificial carbon powder bed with the LSTO green body embedded; these three samples are labeled LSTO-$H_2$, LSTO-$H_2$-C, and LSTO-$H_2$-in-C, respectively. To create more oxygen vacancies, the sintering time (24 h) for the LSTO-$H_2$-C and LSTO-$H_2$-in-C samples is longer than that of LSTO-$H_2$ (12 h). The oxygen scavenging carbon powder bed is made of the aforementioned LSTO power + 5 wt % GNPs. After sintering, the as-formed pellets were cooled in the corresponding environments to room temperature and then cut into bars and discs of appropriate sizes for detailed characterization.

**Characterization.** The density ($\rho$) of the LSTO ceramic was determined using the Archimedes method. The crystal structure and lattice parameters were characterized by X-ray diffraction (XRD) using a Philips X'Pert diffractometer with the Cu K$\alpha$ source ($\lambda_{Cu\ K\alpha}$ = 1.540598 Å). A continuous scan between 20 and 100° was recorded using 0.0167° step size and a dwell time of 6 s per step. X'Pert HighScore and TOPAS software were used for phase identification and Rietveld refinement. The grain size was undertaken on polished surfaces by scanning electron microscopy (SEM, TESCAN MIRA3 SC FEG-SEM), and the linear intercept method was used to determine the average grain size.[25] X-ray photoelectron spectra (XPS) were collected with a Kratos Axis Ultra spectrometer using monochromatic Al K$\alpha$ radiation ($E_{source}$ = 1486.69 eV). CasaXPS software was used for deconvolution of the Ti 2p core level with a Shirley-type background. Atomic force microscopy (AFM) and KPFM were performed using a JPK NanoWizard 4 XP NanoScience atomic microscope equipped with a Kelvin probe microscopy module. The images were recorded using a Pt−Ir-coated silicon probe (SCM-PIT-V2, Bruker).

**Thermoelectric Measurements.** A ULVAC ZEM-3 system was used to simultaneously determine electrical conductivity and Seebeck coefficients; the measurements were performed at temperatures from 300 to 900 K in a low-pressure helium atmosphere. This inert atmosphere with low oxygen partial pressure, together with the medium−high temperature limit of 900 K, ensures the stability of materials' properties during measurements.[26,27] Thermal diffusivity ($D$) was determined using the laser flash method with a Netzsch LFA-457 laser flash apparatus in an argon atmosphere. Differential scanning calorimetry (Netzsch DSC 404 F1 Pegasus) was used to measure the heat capacity ($C_p$); the measurements were performed in an argon atmosphere. The thermal conductivity ($\kappa$) was obtained from $\kappa = D\rho C_p$.



https://dx.doi.org/10.1021/acsami.0c21699
ACS Appl. Mater. Interfaces 2021, 13, 11879−11890

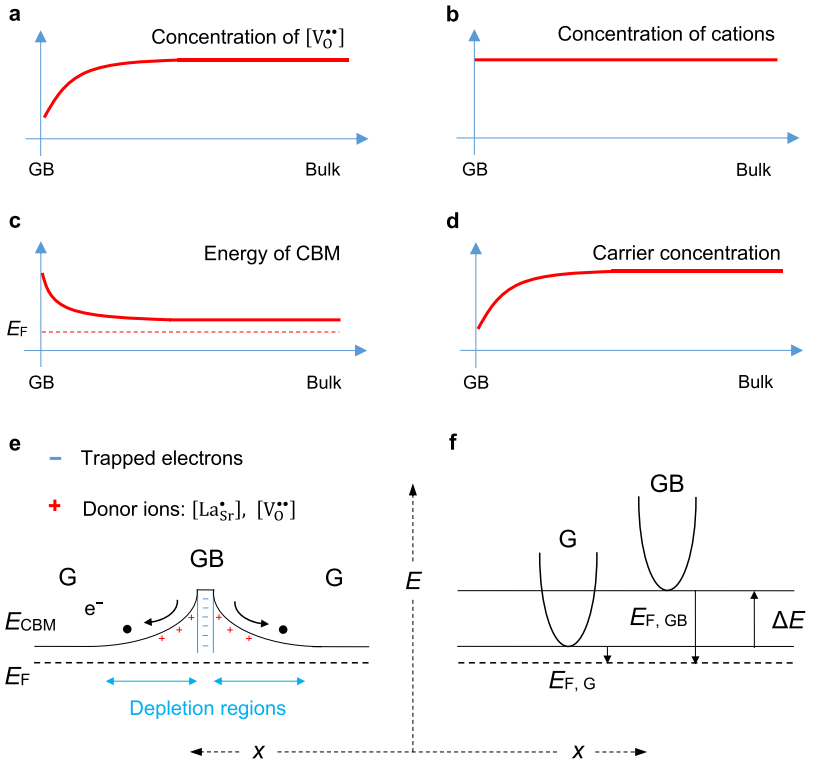


**Figure 1.** Diagrams showing that (a) concentration of oxygen vacancy is lower near the GB compared with the bulk grain, (b) concentrations of cations remain across the GB, (c) CBM bends upward because of the equilibrium of the Fermi energy level, and (d) reduced concentration of the free carrier at the vicinity of the GB. (e) Schematic illustration of the potential barrier across the GB, G represents a neutral grain and the black dots and arrows represent the transport of free electrons being inhibited by the GB barrier. (f) Schematic illustration of the two-phase model for the band offset ($\Delta E$) in the GB phase.

## RESULTS AND DISCUSSION

Figure 1a–d illustrates the way that a negatively charged GB forms and behaves as a potential barrier for electron transport in $SrTiO_3$-based materials. Based upon Snyder's work,[3,7] the formation of a potential barrier in n-type $SrTiO_3$ can be ascribed to the reduction of the concentration of the dominant point defect (oxygen vacancies) near the GB (Figure 1a). Literature results from molecular dynamic simulation also indicate the depletion of oxygen vacancies in regions near dislocation cores,[28] which are analogue lattice defects to the grain boundaries. On the assumption that the concentrations of cations are constant across the GB (Figure 1b), the depletion of positively charged oxygen vacancies (electron-donating defects) near grain boundaries compared to bulk grains induces the difference in Fermi energy levels, promoting electron transfer from the grain to the GB to maintain the equilibrium of the Fermi energy level. This charge transfer leads to a negative potential at the GB region, which alters the local electronic structure at the GB by bending the conductive band upward (Figure 1c).[1,3,29] Energy band diagrams of two grains and their boundary region before and after contact are illustrated in Figure S1a,b, respectively. The trapped electrons at the GB results in much less free carriers in the vicinity of the GB and thus greater resistance compared to the bulk neutral grain (Figure 1d). Figure 1e depicts the overall principle of a GB potential in n-type La-doped $SrTiO_3$ acting as a barrier for majority carrier (i.e., electrons) transport. In addition, the grain boundaries with lattice mismatch act as scattering centers for carrier transport. The combination of a potential barrier and lattice defects at the grain boundaries leads to compromised electrical conductivity compared to that of the bulk neutral grain. The two-phase model treats the GB as a secondary phase with (i) a band offset ($\Delta E$) from the bulk grain phase (Figure 1f), representing the band bending, and (ii) a different carrier scattering mechanism from the bulk grain phase, mimicking carrier scattering, because of the lattice mismatch.

In detail, the Fermi energy level of a GB phase ($E_{F,GB}$) measured from the band edge (CBM: conductive band minimum) is defined by the band offset to be[1]

$$E_{F,GB} = E_{F,G} - \Delta E \quad (1)$$

where $E_{F,G}$ is the Fermi energy level of the grain phase measured from the CBM, positive for free carrier energy that is higher than the CBM energy level.

Since the band offset $\Delta E$ also depends on the doping level of the material, an empirical, linear form of the band offset function can be used to describe the energy dependency of $\Delta E$

$$\Delta E = \Delta E_0 + aE_{F,G} \quad (2)$$

where $\Delta E_0$ is the reference band offset at $E_{F,G} = 0$; it defines the magnitude of the band offset and therefore acts as a modeling parameter in this work; the coefficient $a$ is an empirical parameter which determines the energy dependency of $\Delta E$.

With a known Fermi energy level, the electrical conductivity ($\sigma$) and Seebeck coefficient ($S$) of the grain and GB phases can be calculated by the well-established carrier transport equations[30]

$$\sigma = \sigma_{E_0}(T)sF_{s-1}(\eta) \quad (3)$$


https://dx.doi.org/10.1021/acsami.0c21699
ACS Appl. Mater. Interfaces 2021, 13, 11879–11890

$$S = \frac{k_B}{e}\left[\frac{(s+1)F_s(\eta)}{sF_{s-1}(\eta)} - \eta\right] \quad (4)$$

where the transport coefficient $\sigma_{E_0}(T)$ is a temperature-dependent but energy-independent coefficient that determines the magnitude of electrical conductivity; $T$ is the absolute temperature, $s$ is the transport parameter related to the carrier scattering mechanism; $\eta$ is the reduced Fermi energy level ($\eta = E_F/k_BT$); $k_B$ is the Boltzmann constant; $e$ is the elementary charge, and $F_i(\eta)$ is the Fermi−Dirac integral

$$F_i(\eta) = \int_0^\infty \frac{\epsilon^i}{1 + e^{\epsilon-\eta}}\, d\epsilon \quad (5)$$

where $\epsilon$ is the reduced particle energy ($\epsilon = E/k_BT$; $E$: particle energy).

For the neutral grain phase of $SrTiO_3$ compounds, acoustic phonon scattering ($s = 1$) is assumed to be the dominant carrier scattering mechanism,[7,22] with a crystalline metallic-type temperature dependency of the transport coefficient ($\sigma_{E_0,G}(T) \propto 1/T$; the subscript G denotes the grain phase). Earlier studies suggest that the donor concentration (point defects: $[La_{Sr}^{\bullet}]$ or $[V_O^{\bullet\bullet}]$) dependency of carrier mobility in single-crystal $SrTiO_3$ only becomes significant at low temperatures (e.g., <150 K).[17,31] The present work is focusing on room temperature and above, and thus, the ionic impurity scattering is not included as a scattering source in bulk neutral grain. We verified this assumption by fitting literature data for carrier transport for La- or Nb-doped $SrTiO_3$ single crystals,[32] using the value of $\sigma_{E_0,G}$ at 300 K as a fitting parameter. The modeled results with $\sigma_{E_0,G} = 900$ S cm$^{-1}$ at 300 K (Figure S2) agree well with the reported temperature dependency of electrical conductivity, as well as the log |S| − log $\sigma$ plot. Hence, $s = 1$ and $\sigma_{E_0,G}(T) \propto 1/T$ with a value of 900 S cm$^{-1}$ at 300 K were used as universal modeling parameters for the neutral grain phase in this work. For the GB phase with space charge and lattice mismatch, an ionized-impurity scattering model ($s = 3$; $\sigma_{E_0,GB}(T) \propto T^3$, the subscript GB denotes the GB phase) was used,[1] with $\sigma_{E_0,GB} = 0.15$ S cm$^{-1}$ at 300 K. Table 1 shows the optimized modeling parameters for our materials.

**Table 1. Modeling Parameters for $La_{0.08}Sr_{0.9}TiO_{3-\delta}$ (LSTO) Prepared with Different Sintering Conditions**

| | | band offset function | | transport coefficient (300 K) | |
|---|---|---|---|---|---|
| sample | $t_{GB}$[a] | $a$ | $\Delta E_0$ (meV) | $\sigma_{E_0,G}$ (S cm$^{-1}$) | $\sigma_{E_0,GB}$ (S cm$^{-1}$) |
| LSTO-$H_2$ | 0.001 (1.75 $\mu$m) | 0.3 | 100 | 900 | 0.15 |
| LSTO-$H_2$-C | 0.0005 (3.69 $\mu$m) | | 75 | | |
| LSTO-$H_2$-in-C | 0.0005 (2.67 $\mu$m) | | 10 | | |

[a]The average grain size of the sample is shown in the parenthesis.

A simple series circuit model was used to calculate the overall charge transport behavior; the overall electrical conductivity $\sigma$ was obtained from

$$\frac{1}{\sigma} = \frac{1 - t_{GB}}{\sigma_G} + \frac{t_{GB}}{\sigma_{GB}} \quad (6)$$

where $t_{GB}$ is the size fraction of the GB phase in the ceramic. The value of $t_{GB}$ is proportional to the grain size and thus can be estimated from microstructure characterization. This estimation of $t_{GB}$ from the grain size assumes that the thickness of the carrier-depleted region is consistent for different samples, that is, the thickness of the carrier depletion region is independent of the magnitude of the potential barrier. This assumption is reasonable as the $SrTiO_3$-based ceramics developed for thermoelectric applications have high donor concentrations, typically ~$10^{20}$ cm$^{-3}$; therefore, the charge screening length should be similar. Although a more accurate description of a real GB should correlate the thickness of the depletion region to the magnitude of the potential barrier,[33] we found that the current approximation is sufficiently good to fit the experimental results.

For the overall Seebeck coefficient $S$, in view of the small fraction of the GB phase in the ceramic ($t_{GB} < 0.001$), we followed the recent work of Kuo et al.[1] and assumed

$$S \approx S_G \quad (7)$$

where $S_G$ is the Seebeck coefficient of the bulk grain; see detailed explanations in the Supporting Information and Figure S3. Note that the energy filtering effect of GB barriers on Seebeck coefficients only becomes prominent for nanostructured materials with grain sizes <50 nm or the size fraction of the barrier phase being high.[34,35] The present work focuses on $SrTiO_3$-based ceramics that have grain sizes over 1 $\mu$m, and thus, their Seebeck coefficients should be dominated by carrier concentration. The assumption of $S \approx S_G$ allowed extraction of the reduced Fermi energy level $\eta$ of the grain phase, using eq 4, from the experimentally measured overall Seebeck coefficient of the ceramic. In turn, this allows calculation of the reduced Fermi energy level of the GB phase using eq 1 and 2. Subsequently, the carrier transport characteristic of the polycrystalline $SrTiO_3$ was modeled with only one variable, $\Delta E_0$.

To demonstrate the approach, we modeled the impact of $\Delta E_0$ on the temperature dependencies of electrical conductivity (Figure 2a); the set of Seebeck coefficients for determining the reduced Fermi energy level of the grain phase was obtained from the LSTO-$H_2$ sample that will be discussed later. Obviously, with the decrease in $\Delta E_0$ from 80 to 10 meV, the temperature dependency of conductivity at low temperatures (300−450 K) switches from a thermally activated type to a metallic type. The dramatically enhanced conductivity suggests high power factor values, as the increase in conductivity is due to the change in GB property rather than a change in the carrier concentration of the neutral grain phase (i.e., Seebeck coefficients remain unchanged). The plots of modeled log |S| − log $\sigma$ and power factor—log $\sigma$ (Figure 2b) clearly illustrate the enhancement in the powder factor by reduction of GB barrier heights. For instance, with a Seebeck coefficient of 100 $\mu$V K$^{-1}$, the reduction of $\Delta E_0$ from 80 to 10 meV leads to the enhancement of the power factor from 360 to 1560 $\mu$W m$^{-1}$ K$^{-2}$ (labeled in Figure 2b).

We then fitted literature data for electrical conductivity for $SrTiO_3$-based ceramics,[18,36] using the two-phase model. Typical fitting results are presented in Figure 3. We found that a set of universal fitting parameters ($a = 0.3$, $\Delta E_0 = 100$ meV, $t_{GB} = 0.00025$, $\sigma_{E_0,G} = 900$ S cm$^{-1}$, and $\sigma_{E_0,GB} = 0.15$ S cm$^{-1}$) is sufficient to provide good agreement with the experimental results. In addition, for $La_xSr_{1-y}TiO_3$ with the medium−high doping level ($x = 0.125$ to 0.15), the high


https://dx.doi.org/10.1021/acsami.0c21699
ACS Appl. Mater. Interfaces 2021, 13, 11879−11890

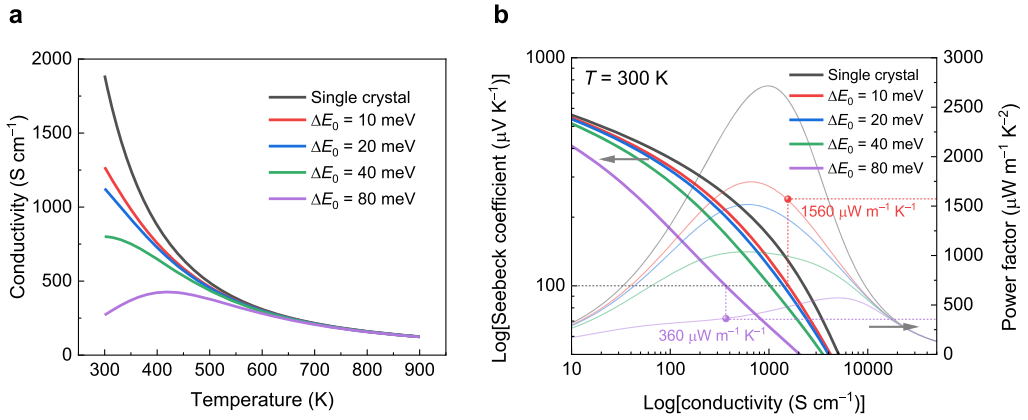


**Figure 2.** Theoretical predictions for GB-dominated charge transport in $SrTiO_3$ ceramics using the two-phase model. (a) Modeled temperature dependency of electrical conductivity for $SrTiO_3$ ceramics with different reference band offset values ($\Delta E_0$) and a fixed $t_{GB}$ value of 0.0005; other parameters ($a$, $\sigma_{E_0,G}$, and $\sigma_{E_0,GB}$) are kept at the universal values shown in Table 1. (b) Simulated log |S| − log $\sigma$ plots (thick solid lines) and plots of the power factor as a function of log $\sigma$ (feint lines) at room temperature (300 K) for $SrTiO_3$ ceramics with different values of $\Delta E_0$. The modeled results for a single crystal ($t_{GB}$ = 0; solid black line) are added for reference purposes.

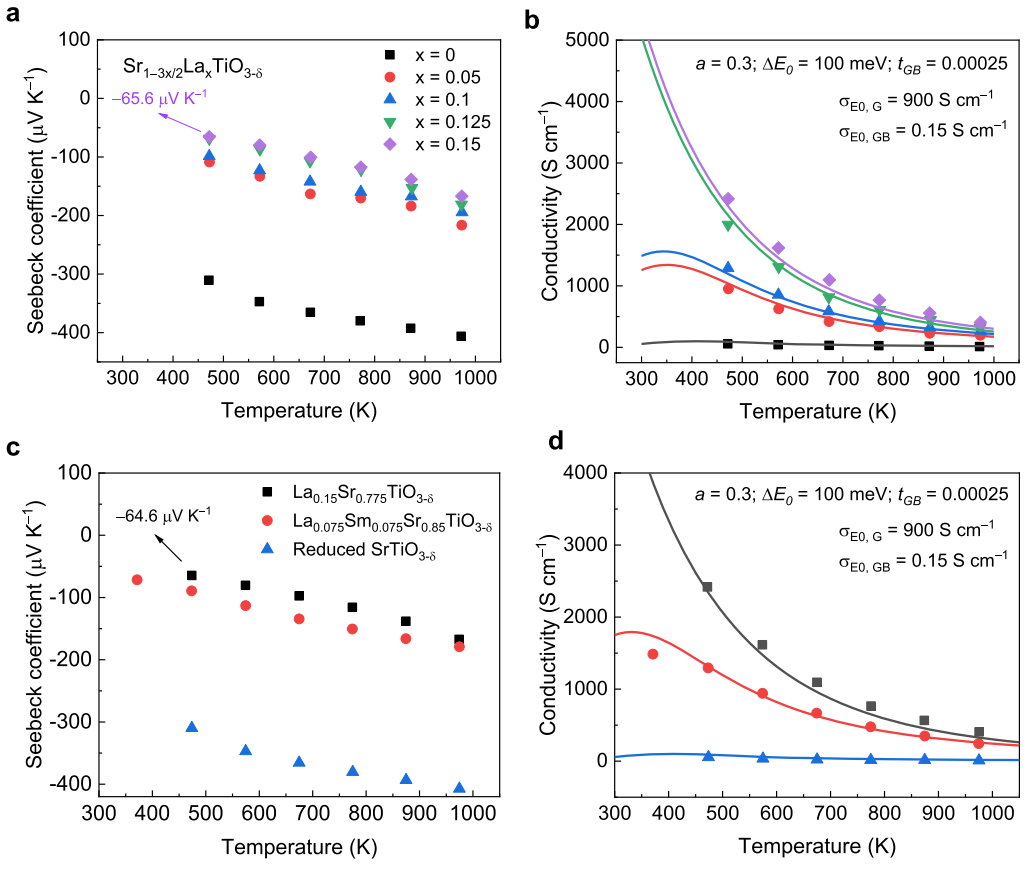


**Figure 3.** Fitting of the measured carrier transport results from the literature using the two-phase model. Experimental data points are displayed as symbols, and the modeled results are shown as solid lines. Data points for Seebeck coefficients (a) and electrical conductivity (b) are from the work of Lu et al.[36] Data points for the Seebeck coefficient (c) and electrical conductivity (d) are from Boston et al.[18]

electrical conductivity due to high carrier concentration overwhelmed GB resistance at low temperatures, leading to a metallic-type conductivity. However, this way of achieving high conductivity at low temperatures, by heavy doping, has the disadvantage that Seebeck coefficients are severely reduced. In fact, a small Seebeck coefficient, down to ~65 $\mu$V K$^{-1}$ at 470 K as shown in Figure 3a,c, is required to give the neutral-grain sufficiently high electrical conductivity to overwhelm the GB resistance at room temperature (Figure 3b,d).

The current literature lacks results from a set of pure $SrTiO_3$-based samples that have the same stoichiometry and comparable Seebeck coefficients, but distinctly different electrical conductivities, to allow a detailed study of GB effects. Nevertheless, an earlier report,[17] together with recent investigations,[3,18,22] of $SrTiO_3$-based electronic ceramics


https://dx.doi.org/10.1021/acsami.0c21699
ACS Appl. Mater. Interfaces 2021, 13, 11879−11890

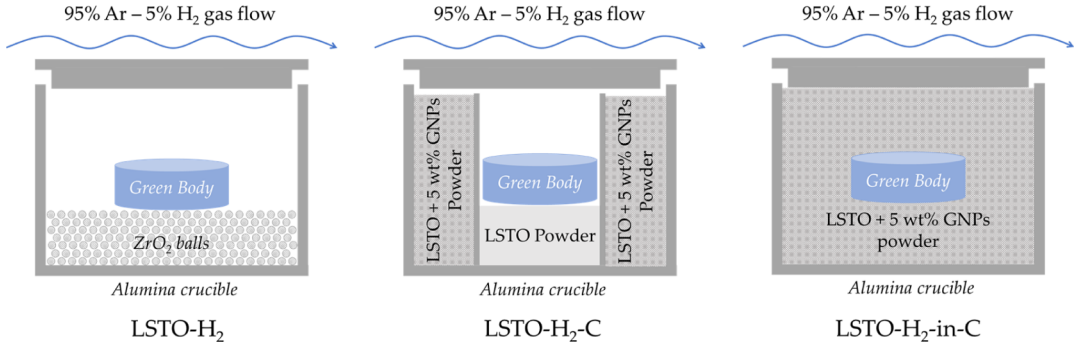


**Figure 4.** Schematic illustrations for the sintering of LSTO ceramics under different conditions with an increasingly strong reducing environment from left to right. The oxygen scavenging sacrificial carbon powder bed is made of LSTO + 5 wt % GNPs.

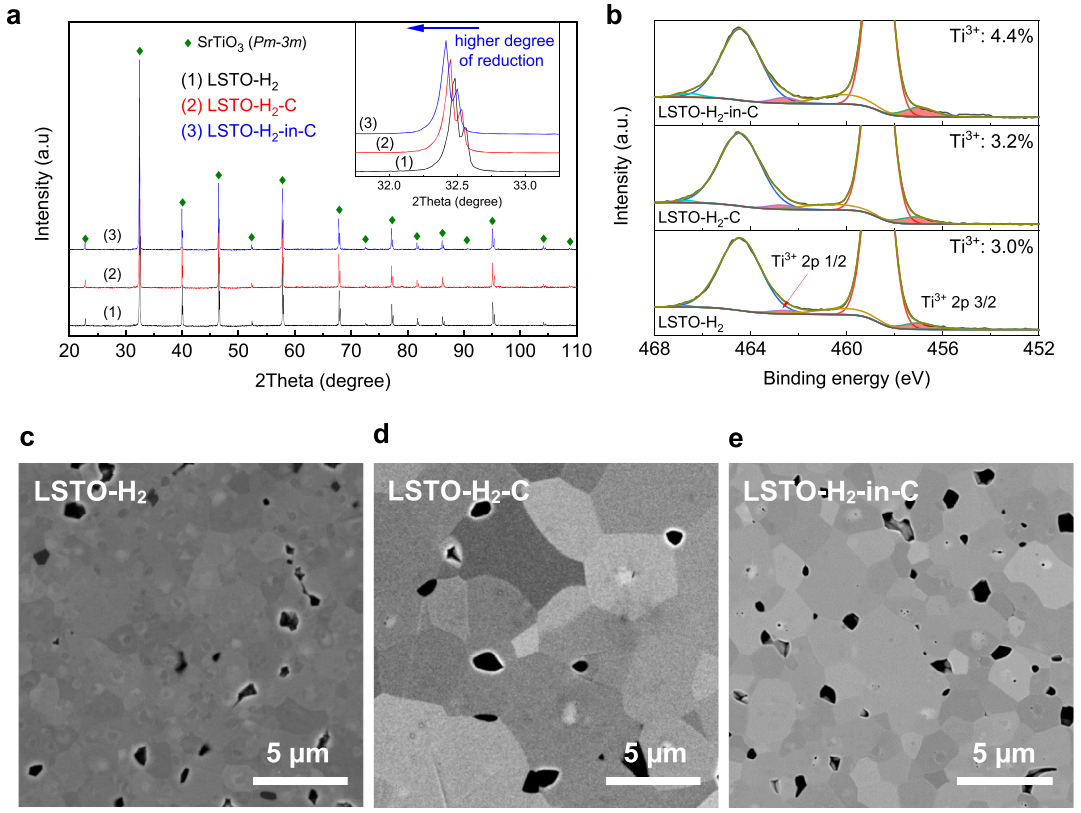


**Figure 5.** Characterization of the LSTO ceramics sintered under three different conditions with an increasingly strong reducing environment. (a) XRD pattern for the three LSTO samples. (b) XPS Ti 2p core levels for the three LSTO samples. (c–e) SEM micrographs showing grain sizes of the LSTO-$H_2$, LSTO-$H_2$-C, and LSTO-$H_2$-in-C samples, respectively.

**Table 2. Carrier Concentration Estimated from the $Ti^{3+}$/Ti and the Corresponding Drift Mobility and Effective Mass at 330 K**

| sample | $a$ (Å) | $Ti^{3+}$/Ti (%) | $n$ ($10^{20}$ $cm^{-3}$) | $\sigma$ (S $cm^{-1}$) | $S$ ($\mu$V $K^{-1}$) | $\mu$ ($cm^2$ $V^{-1}$ $s^{-1}$) | $m^*/m_0$[a] |
|---|---|---|---|---|---|---|---|
| LSTO-$H_2$ | 3.9080 | 3.0 | 5.02 | 85 ± 4 | −129 ± 9 | 1.1 | 3.7 |
| LSTO-$H_2$-C | 3.9087 | 3.2 | 5.39 | 492 ± 25 | −116 ± 8 | 5.7 | 3.5 |
| LSTO-$H_2$-in-C | 3.9095 | 4.4 | 7.36 | 1288 ± 64 | −115 ± 8 | 10.9 | 4.2 |

[a]Free electron mass ($m_0$).

implies that it should be possible to experimentally modulate the GB property by the control of processing conditions (temperature, oxygen partial pressure, etc.). The change in processing conditions, such as a higher temperature and/or more reducing atmosphere with lower oxygen partial pressure, lead to a transformation of low-temperature conductivity from thermally activated to a metallic type.[18,37] This change in conductivity behavior is suspected to be predominantly due to the modulation of grain boundaries (e.g., a localized increase in concentration of oxygen vacancies).[17]

Therefore, we experimentally modulated the GB properties (e.g., oxygen vacancy concentration) of $La_{0.08}Sr_{0.9}TiO_3$ (LSTO) ceramic via control of the reducing strength of the sintering environment (indirect control of oxygen partial pressure). Sample preparation details are illustrated in Figure 4 and described in the Experimental Section. The relative


https://dx.doi.org/10.1021/acsami.0c21699
ACS Appl. Mater. Interfaces 2021, 13, 11879−11890

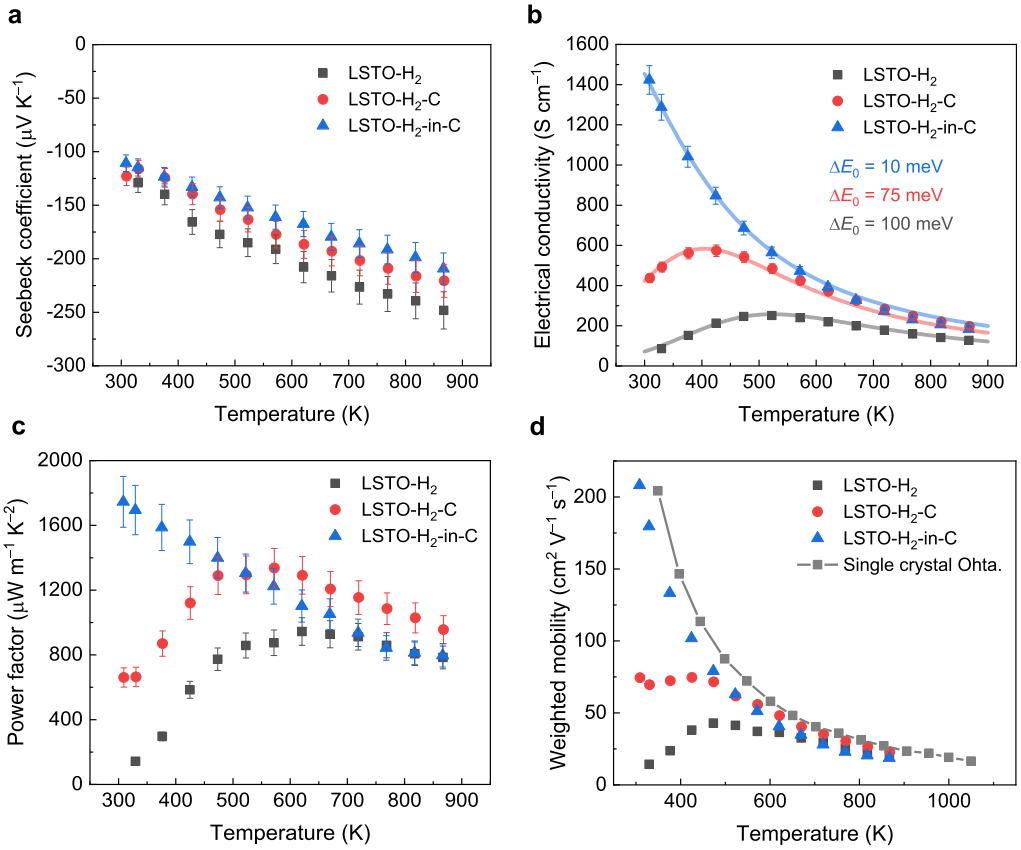


**Figure 6.** Temperature-dependent electric charge transport properties of the as-prepared LSTO ceramic samples; experimental data are represented by solid symbols. (a) Seebeck coefficient and (b) electrical conductivity; solid lines are from the model, using the parameters listed in Table 1; the simulated curves well capture the evolution of electrical conductivity with temperature. (c) Power factor and (d) weighted mobility; the weighted mobility of single-crystal La-doped $SrTiO_3$ calculated from the literature data[32] is included for comparison purposes.

densities for the sintered LSTO-$H_2$, LSTO-$H_2$-C, and LSTO-$H_2$-in C samples are 94.0, 96.0, and 89.3%, respectively.

XRD patterns collected from the three LSTO samples (Figure 5a) show a cubic perovskite structure with $Pm\bar{3}m$ space group symmetry. The decrease in diffraction angle for the samples prepared in more reducing environments (inset of Figure 5a) suggests an increase in the lattice parameter (Table 2). This increase corresponds to an increasing fraction of the small-sized $Ti^{4+}$ (60.5 pm) being converted to relatively larger-sized $Ti^{3+}$ (67 pm).[23] XPS further confirmed the increasing degree of reduction of the LSTO samples from the more reducing environments. The deconvolution of Ti 2p core levels (Figure 5b) leads to quantization of the concentration of $Ti^{3+}$ as a fraction of total Ti, that is, ($Ti^{3+}$/Ti); the $Ti^{3+}$ concentrations for the LSTO-$H_2$, LSTO-$H_2$-C, and LSTO-$H_2$-in-C are 3.0, 3.2, and 4.4%, respectively. This enhancement in the $Ti^{3+}$ concentration implies a higher concentration of oxygen vacancies according to

$$[Ti'_{Ti}] \approx [La^{\bullet}_{Sr}] + 2[V^{\bullet\bullet}_{O}] - 2[V''_{Sr}] \quad (8)$$

The determination of $Ti^{3+}$ concentration also allows the estimation of carrier concentration ($n$) by[38]

$$n = (Ti^{3+}/Ti) \times N_{fu}/V_{uc} \quad (9)$$

where $N_{fu}$ is the number of formula per unit cell (1 for $SrTiO_3$) and $V_{uc}$ is the volume of the unit cell. The calculated results are displayed in Table 2. The LSTO-$H_2$-in-C shows the highest carrier concentration of $7.36 \times 10^{20}$ cm$^{-3}$.

Figure 6 displays the temperature-dependent carrier transport properties for the three LSTO ceramic samples. The absolute value of the Seebeck coefficient (Figure 6a) is slightly lower for the samples sintered in the more reducing environments, corresponding to the higher carrier concentrations implied by the $Ti^{3+}$ concentration (Table 2). In contrast to the relatively small variation in the Seebeck coefficient, the three LSTO samples exhibit distinctly different electrical conductivities, particularly at temperatures below 500 K (Figure 6b). For example, at 330 K, there is over 1 order of magnitude difference in electrical conductivity between the LSTO-$H_2$ (85 S cm$^{-1}$) and the LSTO-$H_2$-in-C (1287 S cm$^{-1}$) samples. Considering the variation of density between these three samples, we estimated their effective conductivities at 330 K following a published approach based on Maxwell equations,[39] see details in the Supporting Information and Table S1. The results show that the effective electrical conductivity is higher than the experimental values, and the conductivity increase due to correction is more pronounced for the samples containing a higher degree of porosity.

In addition to distinct differences in the magnitude of electrical conductivity, the as-prepared samples also show very different temperature dependencies, particularly at low temperature. Both of the LSTO-$H_2$ and LSTO-$H_2$-C samples show a typical GB-dominated, thermally activated conductivity, that is, at low temperatures, the electrical conductivity increases, reaches a maximum, and then decreases at higher temperatures. Due to the larger grain size of LSTO-$H_2$-C and plausibly lower GB potential barrier compared to LSTO-$H_2$,


https://dx.doi.org/10.1021/acsami.0c21699
ACS Appl. Mater. Interfaces 2021, 13, 11879−11890

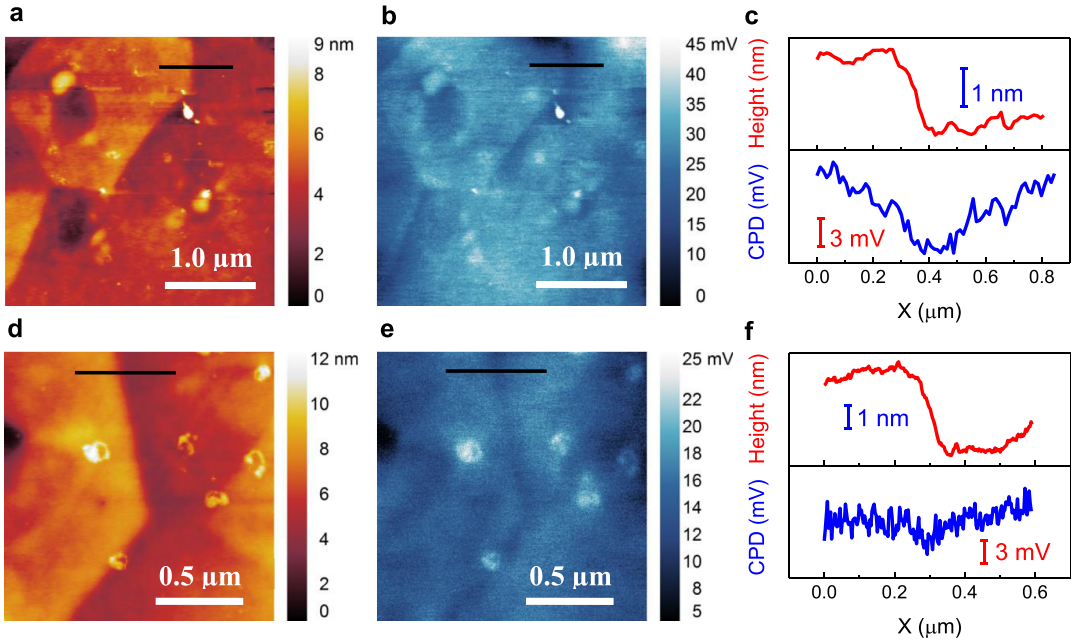


**Figure 7.** AFM and KPFM characterization for the LSTO-$H_2$ and LSTO-$H_2$-in-C samples. (a) AFM height and (b) the corresponding CPD images for the LSTO-$H_2$ sample with high GB potential; (c) extracted height (upper panel) and CPD (lower panel) profiles for the black lines marked in (a,b), respectively. (d) AFM height and (e) the corresponding CPD images for the LSTO-$H_2$-in-C sample with low GB potential; (f) the extracted height (upper panel) and CPD (lower panel) profiles for the black lines marked in (d,e), respectively.

the LSTO-$H_2$-C has higher electrical conductivity at low temperatures and peak electrical conductivity at a lower temperature (smaller thermal energy needed to overcome the GB resistance). More interestingly, although LSTO-$H_2$-in-C has a smaller grain size (2.67 $\mu$m) than that of the LSTO-$H_2$-C (3.69 $\mu$m), the LSTO-$H_2$-in-C sample exhibits a metallic-type (i.e., single-crystal-like) electrical conductivity in the measured temperature range from 300 to 900 K, with the highest conductivity of up to 1423 S $cm^{-1}$ at ~300 K. This switch of temperature dependency is primarily due to the change in the grain boundaries' property (barrier height) rather than the grain size.

To provide further insight into the GB processes, we first calculated the electrical conductivity of the neutral grain phase using eq 3 and the reduced Fermi energy level $\eta$ extracted from the measured Seebeck coefficients (Figure 6a) according to eq 4. The calculated conductivities of the neutral grain phase for the LSTO-$H_2$, LSTO-$H_2$-C, and LSTO-$H_2$-in-C samples are quite similar, particularly the latter two (Figure S4). This decoupling of the neutral-grain-phase electrical conductivity from the measured overall conductivity directly indicates the dominance of grain boundaries in carrier transport in polycrystalline $SrTiO_3$-based ceramics. We subsequently fitted the measured electrical conductivity data with the two-phase model (eq 6), using parameters listed in Table 1; the reduced Fermi energy level of the GB phase was calculated using eq 1 and the band offset function (eq 2), with $\Delta E_0$ as the only fitting parameter. The value of $t_{GB}$ was chosen according to the average grain size from SEM images (Figure 5c–e) and empirically according to the literature,[1] as discussed above, and is therefore considered as a "known" parameter. The solid lines displayed in Figure 6b are from the two-phase model; the simulated results fit well to the measured electrical conductivity. The $\Delta E_0$ values that lead to the best fit of the measured conductivity data are 100, 75, and 10 meV for LSTO-$H_2$, LSTO-$H_2$-C, and LSTO-$H_2$-in-C samples, respectively.

The power factor ($S^2\sigma$) exhibits similar temperature dependency as that of the electrical conductivity (Figure 6c). The LSTO-$H_2$-in-C has the highest power factor value of 1745 $\mu$W $m^{-1}$ $K^{-2}$ at room temperature, an order of magnitude higher than that of the LSTO-$H_2$ sample (143 $\mu$W $m^{-1}$ $K^{-2}$) at 330 K. In addition, the LSTO-$H_2$-C also shows a high power factor value of 1337 $\mu$W $m^{-1}$ $K^{-2}$ at 570 K. These power factor values are among the highest values reported for $SrTiO_3$-based compounds (Table S2).[6,18,20−24,36,38,40−44]

We further computed the weighted mobility ($\mu_w$) of the LSTO samples from the measured electrical conductivity and Seebeck coefficients using the approach reported recently by Snyder et al.[7,45] In detail, the LSTO ceramic was treated as a homogeneous phase with acoustic phonon scattering as the dominating scattering mechanism (transport parameter $s = 1$), the reduced Fermi energy level $\eta$ at each temperature was extracted from the Seebeck coefficients using eq 4, and then, the temperature-dependent transport coefficient $\sigma_{E_0}(T)$ was computed according to eq 3. The determination of the transport coefficient $\sigma_{E_0}(T)$ then leads to the calculation of weighted mobility by

$$\sigma_{E_0} = \frac{8\pi e(2m_e k_B T)^{3/2}}{3h^3}\mu_w \tag{10}$$

where $m_e$ is the free electron mass and $h$ is the Plank constant. This weighted mobility is temperature-dependent but energy- and carrier concentration-independent and allows a direct comparison of carrier mobility for samples at various doping levels. The comparison of weighted mobility derived from the literature data for $SrTiO_3$-based single crystals[32] shows similar values of weighted mobility, regardless of the doping concentration (Figure S5). Figure 6d shows the computed $\mu_w$ for the three LSTO samples prepared in the present work.



https://dx.doi.org/10.1021/acsami.0c21699
ACS Appl. Mater. Interfaces 2021, 13, 11879−11890

Significant enhancement of $\mu_w$ is obvious for the LSTO prepared in the most reducing environment; it has the smallest $\Delta E_0$ value from the two-phase model. Excitingly, the LSTO-$H_2$-in-C sample with a metallic-type electrical conductivity at the measured temperature range exhibits a weighted mobility approaching that of the single crystal (Figure 6d).

The carrier concentration $n$ determined from compositional data by eq 9 also allows the estimation of drift mobility ($\mu$) from the measured electrical conductivity using the Drude–Sommerfeld free-electron model

$$\sigma = ne\mu \tag{11}$$

Furthermore, with the parabolic band and energy-independent scattering approximation, the carrier effective mass ($m^*$) was estimated from the measured Seebeck coefficients by[38]

$$S = \frac{8\pi^2 k_B^2}{3eh^2} m^* T \left(\frac{\pi}{3n}\right)^{2/3} \tag{12}$$

The estimated values of $\mu$ and $m^*$ at 330 K are presented in Table 2. It is interesting to note that the best performing LSTO-$H_2$-in-C sample shows the highest effective mass ($m^*/m_0$ = 4.2) and highest drift mobility ($\mu$ = 10.9) among the three measured samples. These values are comparable to literature values reported for mobility ($\mu$ = 9.2) and effective mass ($m^*/m_0$ = 6.0) for a single crystal with a similar carrier concentration ($n = 6.8 \times 10^{20}$ cm$^{-3}$) at room temperature.[32]

The carrier transport and modeling results strongly indicate a reduction of the height of potential barriers at grain boundaries. To verify this reduction of the potential barrier, we used KPFM, also known as scanning surface potential microscopy, to characterize the contact potential difference (CPD) across the grain boundaries. The AFM height images of the sample surface were collected simultaneously during the KPFM measurement. Figure 7 presents the height and CPD images collected from the LSTO-$H_2$ (Figure 7a,b) and LSTO-$H_2$-in-C (Figure 7d,e) samples. The grain boundaries are clearly distinguishable in both the height and CPD images due to the height variation of adjacent grains and the existence of potential barriers at the grain boundaries, respectively. The height profiles (Figure 7c,f) extracted from the lines marked in Figure 7a,d indicate a well-defined stair feature, showing a height variation of around 2 nm between the adjacent grains. In contrast, the profiles of CPD do not follow that of the topography but exhibit a valley at the GB region, suggesting negatively charged grain boundaries as expected.

More importantly, the magnitude of this negatively charged potential barrier at the GB clearly differs between the two measured samples, ~6 mV for the LSTO-$H_2$ sample and <3 mV for the LSTO-$H_2$-in-C. The smaller magnitude of negative potential at the GB of LSTO-$H_2$-in-C compared to that of the LSTO-$H_2$ sample correlates well with differences in their temperature dependency of conductivity and the $\Delta E_0$ values from the two-phase model (Figure 6b). Obviously, the measurement of surface potential by KPFM provides direct evidence that the LSTO-$H_2$-in-C sample with a single-crystal-like carrier transport behavior has a smaller potential barrier at the grain boundaries than the LSTO-$H_2$ with thermally activated conductivity. Nevertheless, there is a discrepancy between specific values of the measured potential barrier (several mV in scale) by KPFM and the band offset $\Delta E$ (10–100 meV) from the fitting of electrical conductivity with the two-phase model. This discrepancy is probably due to charge accumulation at the sample surface and the resolution limit of KPFM, causing the lowering and widening of the potential profile.[46]

The two-phase model successfully reproduced the temperature-dependent electrical conductivity of the LSTO samples with the $\Delta E_0$ defining the magnitude of band offset as the only fitting parameter. The measurement of GB potential by KPFM confirmed the soundness of using the magnitude of the band offset (i.e., potential barrier height) at the GB as a fitting parameter. We further simulated plots of (i) log |S| − log $\sigma$ and (ii) power factor as a function of log $\sigma$ at a temperature of 330 K, using the parameters listed in Table 1. The simulated plots are presented as lines in Figure 8; the symbols are experimental

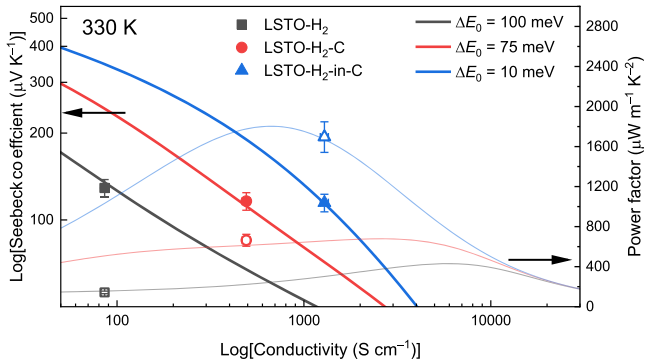


**Figure 8.** Modeled plots of (i) log Seebeck coefficients as a function of log electrical conductivity (thick solid lines) and (ii) power factor as a function of log electrical conductivity (feint lines) at room temperature (330 K) for the three LSTO ceramic samples prepared in the present work. The symbols are experimental results of log |S| − log $\sigma$ (solid symbols) and power factor vs log $\sigma$ (open symbols).

values from the three LSTO samples prepared in this work. The simulated plots fit well with the experimental results. According to Figure 8, it is clear that we achieved an order of magnitude enhancement in electrical conductivity with only minor sacrifice of Seebeck coefficients by the modulation of GB properties. This conductivity enhancement further leads to an order of magnitude increase in power factor. Nevertheless, the power factor of the LSTO ceramic has not yet fully approached that of the single crystal. On the basis of the two-phase model, further enhancement of the power factor is achievable by reduction of the size fraction of GB phase $t_{GB}$ and/or the increase in the transport coefficient of the GB phase $\sigma_{E_0,GB}$.

According to this significant enhancement of the power factor at room temperature, the $ZT$ value of LSTO-$H_2$-in-C increases by an order of magnitude to 0.07 from that of LSTO-$H_2$ (0.007) at 330 K (Figure S6). To achieve a high $ZT$ value, it is necessary to reduce/maintain thermal conductivity of LSTO at a relatively low level while enhancing its electrical conductivity. Ideally, the lattice contribution to the thermal conductivity should remain unchanged when the electronic transport behavior switches from a thermally activated to a single-crystal-like behavior. From the Wiedemann–Franz law, we estimated the electronic contribution ($\kappa_{electronic}$) of the thermal conductivity by $\kappa_{electronic} = L\sigma T$, where $L$ is the Lorenz number and is determined by the transport equation (single parabolic band, acoustic phonon scattering $s$ = 1)


https://dx.doi.org/10.1021/acsami.0c21699
ACS Appl. Mater. Interfaces 2021, 13, 11879–11890

$$L = \left(\frac{k_B}{e}\right)\frac{s(s+2)F_{s-1}(\eta)F_{s+1}(\eta) - (s+1)^2F_s^2(\eta_i)}{s^2F_{s-1}^2(\eta_i)} \quad (13)$$

The reduced Fermi energy level $\eta$ at each temperature was extracted from measured Seebeck coefficients according to eq 4. The lattice contribution ($\kappa_{lattice}$) to the total thermal conductivity ($\kappa_{total}$) is obtained by $\kappa_{lattice} = \kappa_{total} - \kappa_{electronic}$.

This deconvolution of electronic and lattice contributions to the total thermal conductivity (Figure S7a,b) indicates that the higher total thermal conductivity of LSTO-$H_2$-in-C (8.1 W $m^{-1}$ $K^{-1}$) compared to that of LSTO-$H_2$ (6.9 W $m^{-1}$ $K^{-1}$) at 323 K is primarily due to the electronic contribution (0.8 W $m^{-1}$ $K^{-1}$). This much reduced impact of GB modulation on the lattice thermal conductivity compared to electrical conductivity implies an opportunity to achieve the ultimate "phonon glass electron crystal" target by grain size refinement. Earlier work demonstrated a room temperature thermal conductivity as low as 1.2 W $m^{-1}$ $K^{-1}$ for La-doped (10 at %) $SrTiO_3$ ceramic with a grain size of 24 nm.[9] Moreover, for nanostructured materials with a grain size of <50 nm, energy filtering effects become predominant.[34,35] An earlier computational study indicates an opportunity to enhance both the Seebeck coefficient and power factor via the energy filtering effect by a precise control of both the barrier height and grain size, the optimum barrier height being around $k_BT$, ~26 meV at room temperature,[35] which is close to the modeled value in this work for the LSTO-$H_2$-in-C sample (10 meV). However, the creation of a sufficiently high concentration of oxygen vacancies at the grain boundaries requires high temperature and long-term annealing of LSTO in low oxygen partial pressure environments, which is in conflict with the need to limit grain growth. This challenging target might be achievable via the advancement of ceramic processing technologies and/or development of composites in which the secondary components (e.g., graphene) restrain grain growth, while facilitating the creation of oxygen vacancies at the GB.[6,7,22,40,43]

## CONCLUSIONS

We have shown that by both experimental results and modeling, the modulation of the built-in electrostatic potential at the grain boundaries of $SrTiO_3$ leads to charge carrier transport approaching that of single crystals. The two-phase model successfully accounted for the GB potential as a band offset from the neutral grain, highlighting its dominant role in tuning the low-temperature dependency of electrical conductivity. The model showed good agreement with the properties of experimentally prepared LSTO samples that exhibit gradual changes in electrical conductivity behavior from the thermally activated to single-crystal type. KPFM imaging of the surface potential further confirmed the reduced GB potential for LSTO samples with single-crystal-like carrier transport behavior. The successful modulation of GB charge transport leads to an order of magnitude enhancement in the power factor value from 143 to 1745 $\mu$W $m^{-1}$ $K^{-2}$ at 330 K. This work provided further insights and understanding of GB effects on the electrical charge transport in polycrystalline $SrTiO_3$ perovskite and guidance in the design of effective routes to further enhance performance via GB engineering.

## ASSOCIATED CONTENT

### Supporting Information

The Supporting Information is available free of charge at https://pubs.acs.org/doi/10.1021/acsami.0c21699.

Additional modeling details for Seebeck coefficients in the series circuit model; computation of porosity corrected, effective electrical conductivity; energy band diagrams of two grains and their boundary region before and after contact; fitting of the literature reported single-crystal carrier transport data with the carrier transport equations; plot of the total Seebeck coefficient as a function of $t_{GB}$ in the series circuit model; decoupled electric conductivity of the neutral grain phase as a function of temperature for the LSTO samples; weighted mobility of literature-reported La- or Nb-doped single crystals; dimensionless figure of merit for the LSTO samples; and total, lattice, and electronic thermal conductivity for the LSTO samples (PDF)

## AUTHOR INFORMATION


### Corresponding Authors

**Ian A. Kinloch** − *Department of Materials, University of Manchester, Manchester M13 9PL, U.K.; National Graphene Institute and Henry Royce Institute, University of Manchester, Manchester M13 9PL, U.K.;* orcid.org/0000-0003-3314-6869; Email: ian.kinloch@manchester.ac.uk

**Robert Freer** − *Department of Materials, University of Manchester, Manchester M13 9PL, U.K.;* orcid.org/0000-0003-1100-8975; Email: robert.freer@manchester.ac.uk

### Authors

**Jianyun Cao** − *Department of Materials, University of Manchester, Manchester M13 9PL, U.K.; National Graphene Institute and Henry Royce Institute, University of Manchester, Manchester M13 9PL, U.K.;* orcid.org/0000-0003-3437-9947

**Dursun Ekren** − *Department of Materials, University of Manchester, Manchester M13 9PL, U.K.; Department of Metallurgy and Materials Engineering, Iskenderun Technical University, Iskenderun 31200, Hatay, Turkey*

**Yudong Peng** − *Department of Materials, University of Manchester, Manchester M13 9PL, U.K.*

**Feridoon Azough** − *Department of Materials, University of Manchester, Manchester M13 9PL, U.K.*

Complete contact information is available at: https://pubs.acs.org/10.1021/acsami.0c21699


### Author Contributions

J.C. and D.E. contributed equally to this work. The manuscript was written through contributions of all authors. All authors have given approval to the final version of the manuscript.

### Notes

The authors declare no competing financial interest.

## ACKNOWLEDGMENTS

The authors are grateful to the EPSRC for the provision of funding for this work (EP/H043462, EP/I036230/1, EP/L014068/1, and EP/L017695/1 acknowledged by R.F.). J.C. and I.A.K. acknowledge the European Union's Horizon 2020 research and innovation program under grant agreements no. 785219 and 881603. I.A.K. acknowledges Morgan Advanced Materials and the Royal Academy of Engineering for funding

his chair. The work was also supported by the Henry Royce Institute for Advanced Materials, funded through EPSRC grants EP/R00661X/1, EP/S019367/1, EP/P025021/1, and EP/P025498/1. We gratefully acknowledge the support from X-ray facilities in Department of Materials in the University of Manchester. All research data supporting this work are directly available within this publication.

## REFERENCES

(1) Kuo, J. J.; Kang, S. D.; Imasato, K.; Tamaki, H.; Ohno, S.; Kanno, T.; Snyder, G. J. Grain Boundary Dominated Charge Transport in $Mg_3Sb_2$-Based Compounds. *Energy Environ. Sci.* **2018**, *11*, 429−434.

(2) Xu, X.; Liu, Y.; Wang, J.; Isheim, D.; Dravid, V. P.; Phatak, C.; Haile, S. M. Variability and Origins of Grain Boundary Electric Potential Detected by Electron Holography and Atom-Probe Tomography. *Nat. Mater.* **2020**, *19*, 887−893.

(3) Dylla, M. T.; Kuo, J. J.; Witting, I.; Snyder, G. J. Grain Boundary Engineering Nanostructured $SrTiO_3$ for Thermoelectric Applications. *Adv. Mater. Interfaces* **2019**, *6*, 1900222.

(4) Raghuwanshi, M.; Wuerz, R.; Cojocaru-Mirédin, O. Interconnection between Trait, Structure, and Composition of Grain Boundaries in Cu(In,Ga)$Se_2$ Thin-Film Solar Cells. *Adv. Funct. Mater.* **2020**, *30*, 2001046.

(5) Youssef, K. M.; Scattergood, R. O.; Linga Murty, K.; Koch, C. C. Ultratough Nanocrystalline Copper with a Narrow Grain Size Distribution. *Appl. Phys. Lett.* **2004**, *85*, 929−931.

(6) Rahman, J. U.; Du, N. V.; Nam, W. H.; Shin, W. H.; Lee, K. H.; Seo, W. S.; Kim, M. H.; Lee, S. Grain Boundary Interfaces Controlled by Reduced Graphene Oxide in Nonstoichiometric $SrTiO_{3-\delta}$ Thermoelectrics. *Sci. Rep.* **2019**, *9*, 8624.

(7) Lin, Y.; Dylla, M. T.; Kuo, J. J.; Male, J. P.; Kinloch, I. A.; Freer, R.; Snyder, G. J. Graphene/Strontium Titanate: Approaching Single Crystal−Like Charge Transport in Polycrystalline Oxide Perovskite Nanocomposites through Grain Boundary Engineering. *Adv. Funct. Mater.* **2020**, *30*, 1910079.

(8) Avila-Paredes, H. J.; Choi, K.; Chen, C.-T.; Kim, S. Dopant-Concentration Dependence of Grain-Boundary Conductivity in Ceria: A Space-Charge Analysis. *J. Mater. Chem.* **2009**, *19*, 4837−4842.

(9) Buscaglia, M. T.; Maglia, F.; Anselmi-Tamburini, U.; Marré, D.; Pallecchi, I.; Ianculescu, A.; Canu, G.; Viviani, M.; Fabrizio, M.; Buscaglia, V. Effect of Nanostructure on the Thermal Conductivity of La-Doped $SrTiO_3$ Ceramics. *J. Eur. Ceram. Soc.* **2014**, *34*, 307−316.

(10) Bell, L. E. Cooling, Heating, Generating Power, and Recovering Waste Heat with Thermoelectric Systems. *Science* **2008**, *321*, 1457−1461.

(11) Snyder, G. J.; Toberer, E. S. Complex Thermoelectric Materials. *Nat. Mater.* **2008**, *7*, 105−114.

(12) Koumoto, K.; Terasaki, I.; Funahashi, R. Complex Oxide Materials for Potential Thermoelectric Applications. *MRS Bull.* **2011**, *31*, 206−210.

(13) Heremans, J. P.; Dresselhaus, M. S.; Bell, L. E.; Morelli, D. T. When Thermoelectrics Reached the Nanoscale. *Nat. Nanotechnol.* **2013**, *8*, 471−473.

(14) Mori, T.; Priya, S. Materials for Energy Harvesting: At the Forefront of a New Wave. *MRS Bull.* **2018**, *43*, 176−180.

(15) Petsagkourakis, I.; Tybrandt, K.; Crispin, X.; Ohkubo, I.; Satoh, N.; Mori, T. Thermoelectric Materials and Applications for Energy Harvesting Power Generation. *Sci. Technol. Adv. Mater.* **2018**, *19*, 836−862.

(16) Soleimani, Z.; Zoras, S.; Ceranic, B.; Shahzad, S.; Cui, Y. A Review on Recent Developments of Thermoelectric Materials for Room-Temperature Applications. *Sustain. Energy Technol. Assess.* **2020**, *37*, 100604.

(17) Moos, R.; Härdtl, K. H. Electronic Transport Properties of $Sr_{1-x}La_xTiO_3$ Ceramics. *J. Appl. Phys.* **1996**, *80*, 393−400.

(18) Boston, R.; Schmidt, W. L.; Lewin, G. D.; Iyasara, A. C.; Lu, Z.; Zhang, H.; Sinclair, D. C.; Reaney, I. M. Protocols for the Fabrication, Characterization, and Optimization of N-Type Thermoelectric Ceramic Oxides. *Chem. Mater.* **2017**, *29*, 265−280.

(19) Kuo, J. J.; Yu, Y.; Kang, S. D.; Cojocaru-Mirédin, O.; Wuttig, M.; Snyder, G. J. Mg Deficiency in Grain Boundaries of n-Type $Mg_3Sb_2$ Identified by Atom Probe Tomography. *Adv. Mater. Interfaces* **2019**, *6*, 1900429.

(20) Wang, J.; Zhang, B.-Y.; Kang, H.-J.; Li, Y.; Yaer, X.; Li, J.-F.; Tan, Q.; Zhang, S.; Fan, G.-H.; Liu, C.-Y.; Miao, L.; Nan, D.; Wang, T.-M.; Zhao, L.-D. Record High Thermoelectric Performance in Bulk $SrTiO_3$ Via Nano-Scale Modulation Doping. *Nano Energy* **2017**, *35*, 387−395.

(21) Li, J.-B.; Wang, J.; Li, J.-F.; Li, Y.; Yang, H.; Yu, H.-Y.; Ma, X.-B.; Yaer, X.; Liu, L.; Miao, L. Broadening the Temperature Range for High Thermoelectric Performance of Bulk Polycrystalline Strontium Titanate by Controlling the Electronic Transport Properties. *J. Mater. Chem. C* **2018**, *6*, 7594−7603.

(22) Lin, Y.; Norman, C.; Srivastava, D.; Azough, F.; Wang, L.; Robbins, M.; Simpson, K.; Freer, R.; Kinloch, I. A. Thermoelectric Power Generation from Lanthanum Strontium Titanium Oxide at Room Temperature through the Addition of Graphene. *ACS Appl. Mater. Interfaces* **2015**, *7*, 15898−15908.

(23) Okhay, O.; Zlotnik, S.; Xie, W.; Orlinski, K.; Hortiguela Gallo, M. J.; Otero-Irurueta, G.; Fernandes, A. J. S.; Pawlak, D. A.; Weidenkaff, A.; Tkach, A. Thermoelectric Performance of Nb-Doped $SrTiO_3$ Enhanced by Reduced Graphene Oxide and Sr Deficiency Cooperation. *Carbon* **2019**, *143*, 215−222.

(24) Park, K.; Son, J. S.; Woo, S. I.; Shin, K.; Oh, M.-W.; Park, S.-D.; Hyeon, T. Colloidal Synthesis and Thermoelectric Properties of La-Doped $SrTiO_3$ Nanoparticles. *J. Mater. Chem. A* **2014**, *2*, 4217−4224.

(25) Mendelson, M. I. Average Grain Size in Polycrystalline Ceramics. *J. Am. Ceram. Soc.* **1969**, *52*, 443−446.

(26) Sharma, P. A.; Brown-Shaklee, H. J.; Ihlefeld, J. F. Oxygen Partial Pressure Dependence of Thermoelectric Power Factor in Polycrystalline N-Type $SrTiO_3$: Consequences for Long Term Stability in Thermoelectric Oxides. *Appl. Phys. Lett.* **2017**, *110*, 173901.

(27) Ekren, D.; Azough, F.; Gholinia, A.; Day, S. J.; Hernandez-Maldonado, D.; Kepaptsoglou, D. M.; Ramasse, Q. M.; Freer, R. Enhancing the Thermoelectric Power Factor of $Sr_{0.9}Nd_{0.1}TiO_3$ through Control of the Nanostructure and Microstructure. *J. Mater. Chem. A* **2018**, *6*, 24928−24939.

(28) Marrocchelli, D.; Sun, L.; Yildiz, B. Dislocations in $SrTiO_3$: Easy to Reduce but Not So Fast for Oxygen Transport. *J. Am. Chem. Soc.* **2015**, *137*, 4735−4748.

(29) Pike, G. E.; Seager, C. H. The Dc Voltage Dependence of Semiconductor Grain-Boundary Resistance. *J. Appl. Phys.* **1979**, *50*, 3414−3422.

(30) Kang, S. D.; Snyder, G. J. Charge-Transport Model for Conducting Polymers. *Nat. Mater.* **2017**, *16*, 252−257.

(31) Moos, R.; Menesklou, W.; Hardtl, K. H. Hall Mobility of Undoped N-Type Conducting Strontium Titanate Single Crystals between 19 K and 1373 K. *Appl. Phys. A* **1995**, *61*, 389−395.

(32) Ohta, S.; Nomura, T.; Ohta, H.; Koumoto, K. High-Temperature Carrier Transport and Thermoelectric Properties of Heavily La- or Nb-Doped $SrTiO_3$ Single Crystals. *J. Appl. Phys.* **2005**, *97*, 034106.

(33) Kim, S.; Fleig, J.; Maier, J. Space Charge Conduction: Simple Analytical Solutions for Ionic and Mixed Conductors and Application to Nanocrystalline Ceria. *Phys. Chem. Chem. Phys.* **2003**, *5*, 2268−2273.

(34) Thesberg, M.; Kosina, H.; Neophytou, N. On the Effectiveness of the Thermoelectric Energy Filtering Mechanism in Low-Dimensional Superlattices and Nano-Composites. *J. Appl. Phys.* **2016**, *120*, 234302.

(35) Kim, R.; Lundstrom, M. S. Computational Study of Energy Filtering Effects in One-Dimensional Composite Nano-Structures. *J. Appl. Phys.* **2012**, *111*, 024508.



https://dx.doi.org/10.1021/acsami.0c21699
ACS Appl. Mater. Interfaces 2021, 13, 11879−11890

(36) Lu, Z.; Zhang, H.; Lei, W.; Sinclair, D. C.; Reaney, I. M. High-Figure-of-Merit Thermoelectric La-Doped A-Site-Deficient $SrTiO_3$ Ceramics. *Chem. Mater.* **2016**, *28*, 925−935.
(37) Waser, R. Electronic Properties of Grain Boundaries in $SrTiO_3$ and $BaTiO_3$ Ceramics. *Solid State Ionics* **1995**, *75*, 89−99.
(38) Yaremchenko, A. A.; Populoh, S.; Patrício, S. G.; Macías, J.; Thiel, P.; Fagg, D. P.; Weidenkaff, A.; Frade, J. R.; Kovalevsky, A. V. Boosting Thermoelectric Performance by Controlled Defect Chemistry Engineering in Ta-Substituted Strontium Titanate. *Chem. Mater.* **2015**, *27*, 4995−5006.
(39) Zhang, L.; Tosho, T.; Okinaka, N.; Akiyama, T. Thermoelectric Properties of Solution Combustion Synthesized Al-Doped ZnO. *Mater. Trans.* **2008**, *49*, 2868−2874.
(40) Feng, X.; Fan, Y.; Nomura, N.; Kikuchi, K.; Wang, L.; Jiang, W.; Kawasaki, A. Graphene Promoted Oxygen Vacancies in Perovskite for Enhanced Thermoelectric Properties. *Carbon* **2017**, *112*, 169−176.
(41) Kovalevsky, A. V.; Aguirre, M. H.; Populoh, S.; Patrício, S. G.; Ferreira, N. M.; Mikhalev, S. M.; Fagg, D. P.; Weidenkaff, A.; Frade, J. R. Designing Strontium Titanate-Based Thermoelectrics: Insight into Defect Chemistry Mechanisms. *J. Mater. Chem. A* **2017**, *5*, 3909−3922.
(42) Azough, F.; Gholinia, A.; Alvarez-Ruiz, D. T.; Duran, E.; Kepaptsoglou, D. M.; Eggeman, A. S.; Ramasse, Q. M.; Freer, R. Self-Nanostructuring in $SrTiO_3$: A Novel Strategy for Enhancement of Thermoelectric Response in Oxides. *ACS Appl. Mater. Interfaces* **2019**, *11*, 32833−32843.
(43) Wu, C.; Li, J.; Fan, Y.; Xing, J.; Gu, H.; Zhou, Z.; Lu, X.; Zhang, Q.; Wang, L.; Jiang, W. The Effect of Reduced Graphene Oxide on Microstructure and Thermoelectric Properties of Nb-Doped a-Site-Deficient $SrTiO_3$ Ceramics. *J. Alloys Compd.* **2019**, *786*, 884−893.
(44) Teranishi, T.; Ishikawa, Y.; Hayashi, H.; Kishimoto, A.; Katayama, M.; Inada, Y. Thermoelectric Efficiency of Reduced $SrTiO_3$ Ceramics Modified with La and Nb. *J. Am. Ceram. Soc.* **2013**, *96*, 2852−2856.
(45) Snyder, G. J.; Snyder, A. H.; Wood, M.; Gurunathan, R.; Snyder, B. H.; Niu, C. Weighted Mobility. *Adv. Mater.* **2020**, *32*, 2001537.
(46) Kalinin, S. V.; Bonnell, D. A. Screening Phenomena on Oxide Surfaces and Its Implications for Local Electrostatic and Transport Measurements. *Nano Lett.* **2004**, *4*, 555−560.


https://dx.doi.org/10.1021/acsami.0c21699
*ACS Appl. Mater. Interfaces* 2021, 13, 11879−11890